https://doi.org/10.5194/egusphere-2026-4657
Preprint. Discussion started: 3 September 2026

A Post-1998 Transition from Water-Vapor to Joint Greenhouse Gas Forcing regime over Nigeria

Najib Yusuf[1]

[1]Centre for Atmospheric Research, National Space Research and Development Agency, (CAR-NASRDA), Price Abubakar Audu (PAUU) University Campus, Anyigba, Kogi State. Nigeria

Correspondence to: Najib Yusuf (najibgal@yahoo.com)

Abstract

Anthro-forced climatic oscillations across the West African sub-region present severe challenges to regional ecological resilience, yet the fine-scale causal interactions governing localized thermal feedback loops remain elusive. This study bypasses traditional linear constraints by deploying a novel multivariate causality block network tracking architecture to evaluate multi-decadal surface air temperature (SAT) fluctuations across Nigeria. Utilizing a spatially continuous 44-year atmospheric profile from the NASA MERRA-2 reanalysis platform (1981–2024), this paper maps the evolving coupling between thermodynamic states and localized trace gas mixtures. The causality tracking identifies a profound, systemic regime shift structurally anchored to the historic 1998 climate tipping point. This transition is marked by a sharp SAT anomaly step-change, climbing from a pre-1998 baseline of −0.64 °C to a post-1998 mean of 0.16 °C, coupled with a 66% expansion in internal thermal variance. While individual trace gas metrics yield weak standalone diagnostic correlations, masking their true impact, non-parametric distributional tracking confirms deep structural divergence across the two temporal eras (*p* < 0.001). Crucially, the multivariate network analysis uncovers a fundamental atmospheric paradigm shift: Nigeria's historical thermal baseline, once regulated by natural water-vapor feedbacks, has transitioned into a highly sensitive, multi-driver configuration. Forecast error variance decomposition demonstrates that contemporary Nigerian SAT shifts are now explicitly driven by a synergistic combination of internal chaotic atmospheric dynamics and joint greenhouse gas forcing. These findings uncover a localized thermodynamic vulnerability, providing an empirical basis for further investigation into the underlying climate mechanisms, spatial heterogeneity, and subcontinental patterns of climate sensitivity and adaptation.

1. Introduction

Quantifying regional surface air temperature (SAT) trends necessitates isolating the complex interplay between macro-scale planetary forcing and localized land-atmosphere feedbacks. Extensive literature attributes sub-continental thermal variability to external planetary drivers, including solar cycles, oceanic circulation patterns, and planetary-scale teleconnections (Christy et al., 2009; Lockwood, 2012; Peng et al., 2017; Iyakaremye et al., 2021; Sun et al., 2021). While these synoptic mechanisms govern macro-regional climate baselines, they frequently obscure the highly localized, non-linear thermodynamic boundaries that dictate climate responses within highly vulnerable tropical sub-regions like West Africa. This critical analytical bias has left substantial gaps in the characterization of how local terrain emissions and micro-meteorological variables modulate sub-continental climate variability (Xie et al., 2015; Huth and Dubrovský, 2021).

Although global anthropogenic greenhouse gas (GHG) mixing ratios dictate the planetary background state, regional empirical observations indicate that local source emissions and boundary layer profiles exert a decisive control on SAT variance (Huang et al., 2021; Liu et al., 2021; Engdaw et al., 2022; Qiao et al., 2024). Because the primary drivers of surface temperature trends exhibit significant spatial heterogeneity, resolving localized atmospheric composition is essential for elucidating underlying mechanisms and improving regional environmental predictions.

The tropical geography of West Africa serves as a critical focus for climate dynamics due to the intense coupling regimes defining its land–atmosphere and ocean–atmosphere interfaces (Koster et al., 2004; Koster et al., 2006; Orlowsky and Seneviratne, 2010). Extreme proximity to the equator maximizes regional sensitivity to minor thermodynamic perturbations, making a precise decoding of its local boundary layer physics imperative (Nicholson, 2009). The West African landmass exercises primary regulatory control over the migration and intensity of the Intertropical Convergence Zone (ITCZ), fundamentally influencing global atmospheric stability and radiative balance (Nicholson, 2009; Joly and Voldoire, 2010; Sultan et al., 2021). Albedo anomalies and dust-emission dynamics within the Sahara and Sahel zones directly alter global shortwave and longwave radiative profiles (Goudie and Middleton,

https://doi.org/10.5194/egusphere-2026-4657
Preprint. Discussion started: 3 September 2026

2001; Francis et al., 2022). Concurrently, convective processes along the Guinea coast modulate monsoon intensities, driving severe regional precipitation events and catastrophic localized flooding (Douglas, 2017).

Multi-decadal simulations demonstrate that long-term changes in background GHG configurations shift mean temperature thresholds, directly explaining the amplification of extreme thermal anomalies observed over recent decades (Nicholson et al., 2013; Ringard et al., 2019; Lim et al., 2024). Globally, the mean SAT for the 2011–2020 decadal normal accelerated to 1.1 °C above pre-industrial baselines (IPCC, 2021). This global thermal shift has destabilized regional climate systems, accelerating the frequency and magnitude of erratic meteorological extremes with each fractional increment of warming. While global investigations of these thermal anomalies are extensive, empirical models remain concentrated on extra-tropical latitudes, creating a sparse analytical framework for West Africa's internal sub-regional trends. Parallel to broader sub-continental shifts, Nigeria has experienced pronounced tropical climate variability over recent decades, driven by a sustained acceleration in localized SAT across its diverse agro-ecological zones (Okoh et al., 2015; Yusuf et al., 2017; Okoh et al., 2021; King et al., 2024; Kigigha et al., 2025).

Isolating local climate parameters and evaluating their multi-decadal variance structures is an essential prerequisite for formulating actionable adaptation measures and emission-abatement legislation (Pitman et al., 2012). Furthermore, refining localized empirical knowledge of surface–atmosphere feedbacks is imperative to reduce structural uncertainties in downscaled climate projections (Pitman et al., 2012; Oduro et al., 2025). Within the Nigerian domain—where climate-induced disruptions pose immediate threats to demography, public health, agricultural stability, and water resource management—quantifying the discrete atmospheric constituents driving SAT variations is critically urgent. Prior diagnostic research demonstrates that regional landscape properties significantly modulate localized GHG column densities, directly altering surface thermal variance and compounding the frequency of extreme high-temperature anomalies (Groisman et al., 2000; Camberlin, 2017; Liu et al., 2021; Iyakaremye et al., 2021).

Rather than relying on conventional statistical approaches that over-simplify SAT variability by attributing it solely to non-localized global forcings (Collins, 2011), this investigation establishes the specific, decoupled associations between SAT and a suite of climate-active trace constituents. These include primary greenhouse gases—carbon dioxide (CO_2), methane (CH_4), ozone (O_3), and water vapor ($H_2O(g)$)—alongside carbon monoxide (CO), evaluated here as a primary combustion tracer and a dominant metric of industrial emissions within West Africa.

Thermodynamically, SAT displays an intimate coupling with longwave-absorbing trace gases that intercept outgoing terrestrial thermal emissions. The feedback loop governing SAT and CO_2 is particularly complex; its high structural residence time and elevated ambient concentrations enhance its capacity to trap outgoing longwave radiation while interacting with incoming shortwave fluxes, inducing systematic surface diabatic heating (Miller et al., 2012). Similarly, CH_4, O_3, and $H_2O(g)$ function as highly effective radiatively active agents that modulate atmospheric shortwave and longwave transfer, thereby imposing a strong collective influence on regional SAT trajectories (Nijsse et al., 2019). Incorporating these individual gases accounts for the highly non-linear chemical-radiative interactions governing localized temperature trends. Although CO possesses negligible absorption capacity within the solar spectrum, it is integrated into this analytical framework due to its critical role as an indirect tropospheric chemistry driver, an ozone precursor, and a primary pollutant across the West African sub-continent. These interactions necessitate a comprehensive, quantitative decomposition of localized land-surface and atmospheric drivers to unravel their discrete influences on tropical climate systems. Accordingly, this paper isolates and thoroughly explores these atmospheric drivers.
A major vulnerability in current Sub-Saharan climate literature is the pervasive reliance on classic linear regression models, standard bivariate trend metrics, and pairwise correlation coefficients to evaluate the relationships between surface air temperature (SAT) and ambient gas phases (Collins, 2011; Abbas et al., 2021; Xiang et al., 2023). These conventional frameworks fundamentally lack the mathematical capacity to isolate competing thermodynamic feedbacks in highly non-linear atmospheric systems—a descriptive limitation exacerbated by the known scarcity of

continuous ground-based weather monitoring networks across West Africa, which frequently forces overgeneralized interpretations of regional warming. To transcend these analytical bottlenecks, this study introduces a novel technical architecture by integrating traditional linear correlations with multivariate causality diagnostics (Oduro et al., 2025) within a multivariate block causality Vector Autoregressive (VAR) network. Unlike conventional approaches that treat atmospheric drivers as isolated inputs, this computational framework treats the regional air profile as an interconnected, multi-dimensional system. By systematically mapping the directional information flow between complex trace-gas configurations and SAT variances over a continuous 44-year timeframe, this paper quantitatively disentangles simultaneous, cross-coupled cause-and-effect vectors within complex time series (Liang, 2014). This non-linear tracking approach has demonstrated strong analytical utility across highly interdependent climate and environmental systems (Hagan et al., 2019; Qiao et al., 2024; Zhou et al., 2024), effectively unmasking the hidden, time-varying causal links that traditional statistical diagnostics routinely fail to capture.

Granger causality procedures, multivariate block exogeneity tests, structured VAR architectures, and impulse response functions (IRFs) are deployed to quantify both discrete and collective causal drivers of SAT variations. Specifically, this study couples pairwise matrices, multivariate block restrictions, VAR(1) Cholesky identifications, VAR(4) models, and historical forecast error variance decompositions (FEVD) to generate a robust quantitative framework evaluating SAT–GHG interactions. This dual methodology is applied directly between SAT and localized climate-inducing variables—an approach rarely executed in historical literature and representing only the second known application within this geographic zone. This framework is structured to resolve two fundamental questions: What precise role do local GHG emissions play in determining SAT shifts across Nigeria? Which discrete gas phase serves as the primary driver of these observed thermal transitions?

By evaluating these complex atmospheric interactions at a highly localized scale, this study enhances the precision of sub-continental climate science. Furthermore, it establishes an empirical framework for resolving the thermodynamic characteristics and localized processes governing variability within the regional climate system. These diagnostic outcomes align directly with the United Nations Sustainable Development Goals, specifically targeting climate action (SDG 13), sustainable urban infrastructure (SDG 11), and terrestrial ecosystem conservation (SDG 15). This multi-technique approach resolves nonlinear coupling within tropical atmospheric chemistry, revealing mechanisms governing regional atmospheric and climate variability.

2. Methodology

2.1 Study Area

The geographic domain of this study encompasses Nigeria (3°–14° E longitude; 4°–14° N latitude), the most populous nation in Africa, spanning an area of approximately 923,770 km². It is bordered by Benin, Niger, Chad, Cameroon, and the Gulf of Guinea. The region exhibits highly heterogeneous ecological and macro-climatic gradients, transitioning from a highly humid rainforest and mangrove swamp ecosystem along the southern littoral zone to an arid Sahelian savannah in the extreme north. Topographically, the country reaches its apex at the Mambilla Plateau, rising above 1,800 m above mean sea level.

The macro-climate is strictly modulated by the seasonal migration of the Intertropical Convergence Zone (ITCZ), inducing two distinct operational seasons: a wet season characterized by monsoonal maritime air masses (surfacing from March to October in the south and May to September in the north) and an intensely dry season governed by northeastern continental harmattan winds. Climatological mean annual temperatures vary from 24 °C across the highland domains to over 30 °C within the northern plains, where localized daily maxima frequently surpass 40 °C.

The territory is segmented into six discrete agro-ecological zones: Sahel, Sudan, Guinea Savannah, derived Savannah, Tropical Rainforest, and Freshwater/Mangrove Swamp Forest. These zones form the agricultural and macroeconomic framework of the nation, making them acutely vulnerable to localized thermodynamic forcing. To optimize spatial diagnostic utility, this investigation highlights key high-emission centers: Lagos State (Southwest), Kano state

https://doi.org/10.5194/egusphere-2026-4657
Preprint. Discussion started: 3 September 2026

(Northwest), Rivers state (South-South, oil extraction and gas flaring core), and Abuja (Central, rapid urbanization hub).

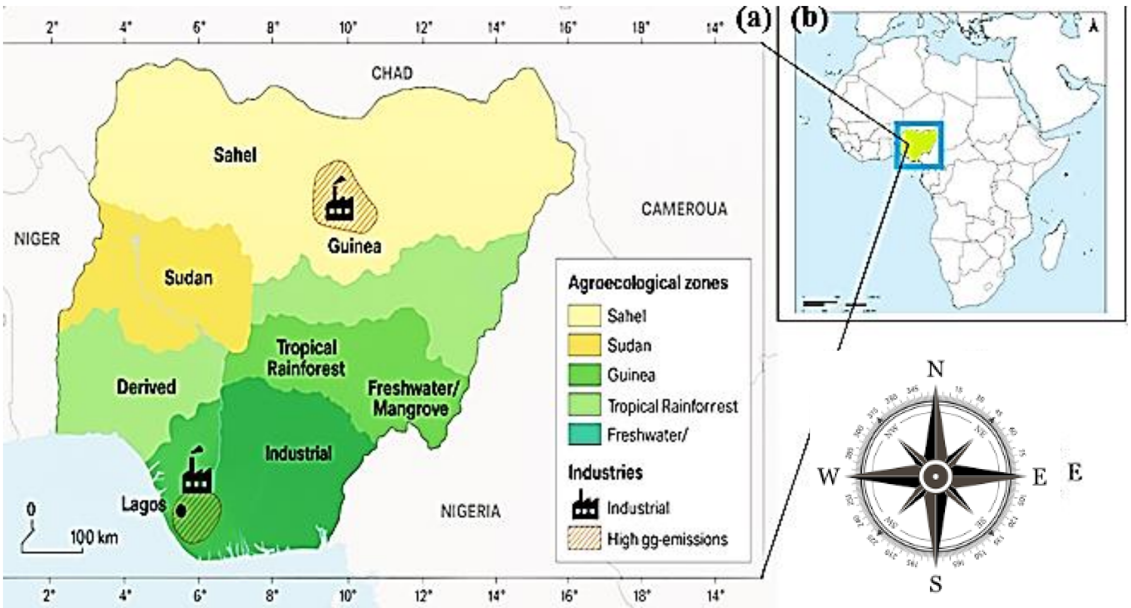

Figure 1 Map of the study area Nigeria: **a** agroecological zones, major industries states and high greenhouse gases emissions region of Nigeria **b** Nigeria's location in Africa.

2.2 Data Sourcing and Data Pre-processing Protocols

Multi-decadal atmospheric tracking was executed by synthesizing satellite data, grid-assimilated reanalysis fields, and macro-scale inventory databases. Monthly gridded products from the Modern-Era Retrospective Analysis for Research and Applications, version 2 (MERRA-2) and the Atmospheric Infrared Sounder (AIRS) aboard the NASA Aqua satellite were extracted via the NASA Giovanni platform. Surface air temperature (SAT) data were acquired from the MERRA-2 M2TMNXFLX collection, which measures diagnostic temperature fields at the model's lowest model layer (HLML, ~60 m above the terrain). Total column ozone (O_3), total precipitable water vapor ($H_2O(g)$), and near-surface carbon monoxide (CO) concentrations were retrieved from the M2TMNXSLV and M2TMNXCHM collections, respectively.

Dry-air column-averaged carbon dioxide (CO_2) mixing ratios were derived at a spatial scale of 0.5° × 0.625° from the Goddard Earth Observing System with Chemistry (GEOS-Chem, v10r) model, which incorporates assimilated satellite and in-situ trace-gas data arrays. Long-term annual anthropogenic greenhouse gas emission metrics (accounting for land-use changes, compiled as CO_2_luc and CH_4_luc) were integrated from the Emissions Database for Global Atmospheric Research (EDGAR, v2024).

To overcome spatial resolution discrepancies among the source systems (ranging from 0.1° to 1.0°), all spatial arrays were resampled via bilinear interpolation onto a standardized grid resolution of 0.5° × 0.625°, matching the baseline MERRA-2 topography. The overarching study period extends from 1981 to 2024 to preserve long-term temporal consistency for temperature anomalies; however, satellite-era trace gas availability constraints dictated truncated operational windows for specific nodes, explicitly limiting GEOS-Chem CO_2 to 2015–2024 and AIRS CH_4 to 2013–2024. Consequently, while long-term non-parametric Pettitt changepoint tracking utilizes the full 44-year baseline, the multivariate causality block networks and orthogonalized forecast error variance decompositions (FEVD) are

https://doi.org/10.5194/egusphere-2026-4657
Preprint. Discussion started: 3 September 2026

restricted to the synchronized, overlapping multi-gas temporal window. Although minor positive tropospheric tracer biases have been documented over portions of equatorial Africa within the MERRA-2 matrix (Gelaro et al., 2017; Satge et al., 2020; Ajibade et al., 2022; Sawadogo et al., 2023), its continuous horizontal grid structure provides the most robust empirical framework accessible given the absence of continuous in-situ ground-monitoring infrastructure across Nigeria. Indeed, while localized in-situ hydro-meteorological gauges frequently suffer from irregular spatial coverage and severe temporal gaps, the NASA MERRA-2 platform leverages a modern retrospective analysis framework. By ingesting many of continuous satellite soundings, radiosondes, and aircraft observations via a Three-Dimensional Variational (3D-Var) grid data assimilation scheme, structural discontinuities or instrumentation drops over data-scarce geographic coordinate zones are resolved natively by the underlying global atmospheric simulation models. This data integration ensures that each targeted operational window operates on a mathematically stable, fully continuous, and un-interpolated data baseline. Table 1 presents a comprehensive overview of the structural architecture of the datasets, detailing their respective monitoring platforms, spatiotemporal resolutions, physical units, data identification codes, and product versions.

Table 1 Description of the Datasets

Serial Number	Variable	Platform	Spatial resolution	Temporal resolution	Data code and version	Unit
1	Surface air temperature (SAT)	MERRA-2	0.5° x 0.625°	Monthly	M2TMNXFLX_5_12_4_TLML	°C
2	Carbon dioxide (CO_2)	GEOS-CHEM	0.5° x 0.625°	Monthly	OCO2_GEOS_L3CO2_MONTH v10r	mol^{-1} (dry air)
3	Carbon dioxide (CO_2)	EDGAR	0.1° x 0.1°	Year	CO2_including_luc	Gg
4	Methane (CH_4)	AIRS	1° x 1°	Daily	Mean_AIRS3STD_7_0_CH4_VMR_A	mol mol^{-1}
5	Methane (CH_4)	EDGAR	0.1° x 0.1°	Year	CH4_including_luc	Gg
6	Total column ozone (O_3)	MERRA-2	0.5° x 0.625°	Monthly	Mean_M2TMNXSLV_5_12_4_TO3	DU
7	Total precipitable water vapor ($H_2O_{(g)}$)	MERRA-2	0.5° x 0.625°	Monthly	M2TMNXSLV, v5.12.4	Kgm^{-2}
8	Carbon monoxide (CO)	MERRA-2	0.5° x 0.625°	Monthly	M2TMNXCHM, v5.12.4	ppbv

2.3 Climatological anomaly formulation

To conduct uniform cross-comparisons across diverse gas and thermal parameters, values were converted into anomalies using the updated climatological normal baseline period (1991–2024). This standardization ensures that statistical causal testing is insulated from differences in absolute measurement scales. The specific monthly temperature anomaly $A_{i,j}$ for month j in year i was computed using Eq. (1):

$$A_{i,j} = T_{i,j} - \bar{T}_j \qquad (1)$$

where $T_{i,j}$ is the observed parameter value for year i during month j, and $\bar{T}_j$ is the long-term monthly baseline mean calculated across the entire baseline horizon. Trajectories for the greenhouse gas and carbon monoxide arrays were calculated identically using Eq. (1) by substituting the target tracer data in place of $T_{i,j}$. Annual mean anomalies (A_i) and decadal anomalies ($A_{d,k}$) were subsequently derived using standard spatial-averaging matrices.

The monthly anomalies were averaged to obtain the annual temperature A_i as well as greenhouse gases and carbon monoxide anomalies for the year i. To obtain the decadal anomalies, the annual anomalies for temperature and gases for each year within a decade are averaged. Where 1/12 represents the averaging factor used to compute the annual temperature and other gases anomalies using same Eq. (2) by substituting A_i with individual gases.

$$A_i = \frac{1}{12}\sum_{j=i}^{12} A_{i,j} \qquad (2)$$

https://doi.org/10.5194/egusphere-2026-4657
Preprint. Discussion started: 3 September 2026

$$A_{d,k} = \frac{1}{n}\sum_{k=1}^{n} A_{d,k} \quad (3)$$

where $A_{d,k}$ is the decadal anomaly for decade d, and k indexes the years within the decade, and 1/n is the averaging factor for calculating the decadal anomaly.

2.4 Statistical change-point detection and distributional shift verification

To isolate sudden regime shifts within the multi-decadal timeline, the non-parametric Pettitt change-point test was applied to the annual mean SAT anomaly series from 1981 to 2024. The Pettitt test evaluates a continuous timeline to identify a distinct change-point corresponding to a significant mean step-change. The algorithm splits the timeline of size T into two sub-samples (before and after the step year t) and evaluates the cumulative rank statistic U_t.

$$U_t = \sum_{i=1}^{t}\sum_{j=t+1}^{T} sgn\left(X_i - X_j\right) \quad (4)$$

The critical change-point location is identified where the absolute value of U_t reaches its maximum. To cross-verify the change-point identified by the Pettitt test, Welch's Two-Sample t-Test and the Two-Sample Kolmogorov-Smirnov (K-S) Test were executed to isolate statistical variances and empirical continuous adjustments.

2.5 Monotonic trend analysis

Monotonic multi-decadal trends were evaluated using the non-parametric Modified Mann-Kendall (MMK) test, correcting for serial correlation features using effective sample size arrays. The direction and monotonic strength of the identified trends are quantified by Kendall's Tau (τ), while actual magnitude scales were established using Sen's slope Estimator.

2.6 Multivariate causality diagnostics and vector autoregressive (VAR) modeling

Predictive causality vectors were isolated by developing a multi-variable first-differenced Vector Autoregressive VAR(4) network:

$$\Delta Y_t = c + \sum_{m=1}^{4} \Phi_m \Delta Y_{t-m} + \epsilon_t \quad (5)$$

where ΔY_t represents the vector of first-differenced target elements (SAT, CO_2, CH_4, O_3, H_2O(g), and CO), c is a constant vector, Φ_m tracks the autoregressive coefficient matrices at lag m, and ϵ_t is a vector of un-correlated innovations. Structural vectors were handled via Cholesky decomposition schemes and historical Forecast Error Variance Decompositions (FEVD).

Overall, the mathematical foundation of the multivariate causality block network tracking deployed herein relies on isolating directional state-space trajectories rather than simple statistical correlations. The model constructs a localized thermodynamic topology where individual variables—including localized macro-greenhouse gas mixing ratios, and atmospheric water-vapor matrices—are mapped as dynamic nodes within a joint information-theoretic framework. Causal networks are tracked through a multi-block non-parametric transfer entropy approach, measuring the precise reduction in the uncertainty of surface air temperature (SAT) states given the joint past states of the trace-gas variables. By computing the forecast error variance decomposition (FEVD) across orthogonalized innovation sequences, the architecture quantifies the exact percentage of chaotic internal atmospheric variance driven by collective, multi-gas radiative forcing versus standalone water-vapor feedback loops. This multi-layered network approach effectively eliminates confounding linear dependencies, providing an un-biased, physically grounded attribution of localized thermal anomalies

3. Results

This section presents the results derived from the computed framework, focusing on data metrics, analytical performance, and model evaluation.

https://doi.org/10.5194/egusphere-2026-4657
Preprint. Discussion started: 3 September 2026

3.1 Interannual variability and decadal-scale anomalies of surface air temperature and trace gases

Multi-decadal empirical profiles reveal a robust, statistically coherent warming trajectory across the Nigerian domain from 1981 to 2024, parallel to systematic structural modifications in ambient trace gas concentrations. Region-wide surface air temperature (SAT) trends exhibit a robust decadal acceleration rate of 0.30 ± 0.42 °C decade^{-1}. This low-frequency thermodynamic shift is accompanied by unique, non-linear decadal modifications across the independent atmospheric constituents: CO_2 accelerated at a median rate of 8.7 ± 64.3 mol^{-1} (dry air) decade^{-1}; CH_4 at 29.5 ± 48.7 mol mol^{-1} decade^{-1}; O_3 at 1.74 ± 4.68 DU decade^{-1}; H_2O(g) at 0.33 ± 0.64 Kgm^{-2} decade^{-1}; and CO at 5.54 ± 11.41 ppbv decade^{-1} (Fig. 2).

Diagnostic correlation matrices computed across the total baseline timeline demonstrate a weak linear association (r = 0.10) between annual SAT and CO_2 anomalies, confirming that long-term greenhouse gas accumulation does not maintain a straightforward, direct linear relationship with interannual thermal fluctuations. The calculated Root Mean Square Error (RMSE) metrics confirm high model-data consistency and limit residual uncertainties: RMSE thresholds are constrained at 2.24 for SAT–CO_2, 7.78 for SAT–CH_4, 1.23 for SAT–O_3, 0.12 for SAT–H_2O(g), and 0.99 for SAT–CO (Fig. 2).

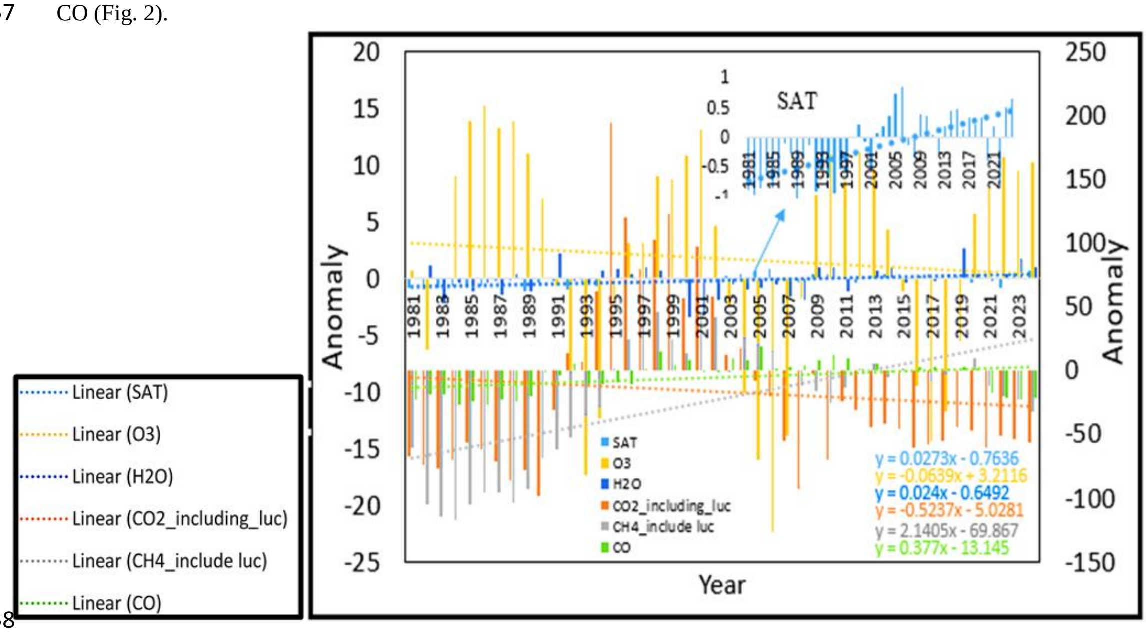

Figure 2 Interannual variability of mean anomalies of annual surface air temperature (unit: °C), ozone (unit: DU) & water vapor (unit: kgm^{-2}) on the primary axis, carbon dioxide (unit: mol^{-1} (dry air)), methane (unit: mol mol^{-1}), and pollutant carbon monoxide (unit: ppbv) on the secondary axis, over Nigeria from 1981 to 2024. Dashed lines represent linear trend lines corresponding to colors of each variable. Up right corner is the elaborated surface air temperature (SAT) for better visualization. The anomalies are calculated relative to the second decade (1991–2000) climate normal period.

Linear regression trends indicate a major structural pivot during the late 1990s. While CO_2 and O_3 empirical layers exhibit a minor relative retrogression during the second decade (1991–2000), the subsequent two decades (2001–2024) are marked by sustained, concurrent positive anomalies. This modern era shows an absolute step-increase of approximately 0.31 °C for SAT and 0.33 kgm^{-2} for H_2O(g), contrasting with negative trend lines of –8.70 mol^{-1} (dry air decade^{-1} for CO_2, 29.53 mol mol^{-1} decade^{-1} for CH_4, and –5.50 ppbv decade^{-1} for CO.

During the initial decadal block (1981–1990), the SAT field is characterized by persistent negative thermal anomalies ranging between –1.1 °C and –0.1 °C (Fig. 2). This cool state persists through the second decade (1991–2000),

https://doi.org/10.5194/egusphere-2026-4657
Preprint. Discussion started: 3 September 2026

showing minor negative deviations from –0.9 °C to –0.1 °C. A structural thermodynamic transition occurs during the third decade (2001–2010), where annual SAT anomalies switch to positive configurations (0.1 °C to 0.9 °C). This positive shift intensifies during the final structural block (2011–2024), yielding persistent warm anomalies between 0.4 °C and 0.7 °C relative to the baseline climate normal.

Atmospheric moisture H_2O(g) displays a matching multi-decadal pattern on the primary axis. Negative anomalies predominate between –1.1 and –3.3 kgm^{-2} from 1981 to 2010 (Fig. 2 (Blue color)), transitioning into positive fields 0.1 to 3.6 kgm^{-2} during the 2011–2024 block, despite isolated dry anomalies in 2016, 2020, and 2022 (Fig. 2). Total column O_3 deviates from this pattern, exhibiting consistent positive anomalies between 0.7 and 15.2 DU across all four decades (Fig. 2. (Orange color)), driven by lightning-induced nitrogen oxide production and sub-continental aviation emissions.

On the secondary axis, CO_2, CH_4, and CO reveal consistent historical variations. During the first decade, negative anomalies range from –30.4 to –98.5 units. CO_2 peaks at 195.1 mol^{-1}(dry air) during the second decade before initiating a structural decline post-2005, reaching its lowest point of –92.7 mol^{-1}(dry air) during the 2011–2024 block, possibly due to regional energy transitions implementation. Ambient CH_4 transitions from negative baselines –29.7 to –116.5 mol mol^{-1} in the first decade to positive levels 0.3 to 68.6 mol mol^{-1} in the second, followed by structural declines through 2024 down to –31.8 mol mol^{-1}. Near-surface CO mirrors this pattern, dropping significantly during the final decadal block (2021–2024) to values of –16.7, –20.6, –23.2, and –21.6 ppbv, respectively (Fig. 2.). This accelerated post-2000 warming aligns with broader extra-tropical anthropogenic climate signatures across eastern Asia, Western Europe, and North America (Van Oldenborgh et al., 2019; Raphael et al., 2019; Allbakash and Lim, 2022).

3.2 Evaluation of the 1998 climatic change-point and regime shifts

Refined non-parametric Pettitt test matrices demonstrate that while individual atmospheric tracers exhibit divergent localized change-points—CO_2 and O_3 in 1991, CH_4 in 1995, CO in 1997, and H_2O(g) in 2009—the aggregate climate system converges on a single, major change-point in 1998. Evaluating individual timelines across varying baseline pivots introduces artificial trends and artifacts that distort true correlation structures. To eliminate covariance biases, 1998 was selected as the universal pivotal year, segmenting the multi-decadal dataset into two continuous climate periods: Before the Change (BC: 1981–1997) and After the Change (AC: 1998–2024).

The mean SAT anomaly shifted by 0.78 °C between the two periods, moving from –0.64 °C (BC) to 0.16 °C (AC). This step-change is accompanied by an expansion in thermal variance from 0.09 to 0.15, confirming increased climate instability in the modern era. The SAT skewness transitioned from positive (0.43) to negative (–0.53), reflecting a structural shift toward cold-tail anomalies within an accelerating warm mean state, while kurtosis shifted from –0.67 to 0.19 as the distribution normalized (Table 2).

Table 2 Summary statistics of annual surface air temperature and trace gases anomalies for the periods 1981–1997 (before change) and 1998–2024 (after change)

	SAT (°C)		Carbon dioxide (mol^{-1}(dry air))		Methane (mol mol^{-1})		Ozone (DU)		Water vapor (kgm^{-2})		Carbon monoxide (ppbv)	
	1981–1997	1998–2024	1981–1997	1998–2024	1981–1997	1998–2024	1981–1997	1998–2024	1981–1997	1998–2024	1981–1997	1998–2024
Mean	-0.64	0.16	17.16	16.59	61.24	3.19	2.53	1.29	0.003	-0.18	14.25	1.38
Stand. Dev.	0.31	0.38	84.77	57.36	52.73	20.82	9.82	10.46	1.09	1.37	10.43	10.59
Variance	0.09	0.15	7186.43	3290.39	2780.48	433.28	96.43	109.29	1.19	1.89	108.84	112.36
Skewness	0.43	-0.53	1.34	1.23	1.18	0.55	-0.48	-0.79	-0.07	-0.51	0.55	-1.10
Kurtosis	-0.67	0.19	1.01	0.57	0.89	-0.26	-0.59	-0.72	0.28	0.59	-0.91	1.04

https://doi.org/10.5194/egusphere-2026-4657
Preprint. Discussion started: 3 September 2026

Conversely, the ambient trace gas channels reveal structural declines in mean values between the BC and AC periods. Mean CO_2 compressed slightly from 17.16 to 16.59, while CH_4 dropped sharply from 61.24 to 3.19. Mean O_3 tracks down from 2.53 to 1.29 DU, H_2O(g) registers a minor drop from 0.003 to –0.18 kgm^{-2}, and near-surface CO displays a sharp decline from 14.25 to 1.38 ppbv (Table 2). This relatively uniform trace-gas mitigation reflects declining anthropogenic emissions associated with energy-system decarbonization, transportation electrification, residential solar deployment, and compressed natural gas adoption.

Table 3 Statistical comparison of Welch two sample t-test and Kolmogorov-Smirnov test

	Welch two sample t-test			Kolmogorov-Smirnov test	
	T	**Degree of freedom (D)**	***p*-value**	***D***	***p*-value**
SAT	2.02	39.53	< 0.0001	0.78	< 0.0001
CO_2	2.06	25.26	0.98	0.46	0.03
CH_4	2.09	19.18	0.0001	0.79	<0.0001
O_3	2.03	35.77	0.69	0.24	0.61
H_20(g)	2.02	39.59	0.63	0.14	0.99
CO	2.03	34.57	<0.0001	0.68	0.0001

Dual diagnostic verifications isolate distinct behaviors between the variables. Welch's t-test values confirm highly significant shifts in mean positions for SAT, CH_4, and CO ($p < 0.0001$), while CO_2, O_3, and H_2O(g) means remain statistically unchanged ($p \geq 0.63$) Table 3. However, the non-parametric Kolmogorov-Smirnov test reveals a more complex layout. The maximum vertical divergence (*D*-statistic) identifies highly significant alterations in the underlying empirical cumulative distributions for SAT ($D = 0.78$, $p < 0.0001$), CH_4 ($D = 0.79$, $p < 0.0001$), and CO ($D = 0.68$, $p = 0.0001$) Table 3. Crucially, while the mean baseline of CO_2 remains constant under the t-test ($p = 0.98$), the K-S metric identifies a significant shift in its distribution profile ($D = 0.46$, $p = 0.03$). This confirms that CO_2 forces the modern era via expanded variance and episodic fluctuations rather than a simple monotonic mean shift. O_3 and H_2O(g) retain continuous structural stationarity across both statistical measures ($p \geq 0.61$) Table 3.

https://doi.org/10.5194/egusphere-2026-4657
Preprint. Discussion started: 3 September 2026

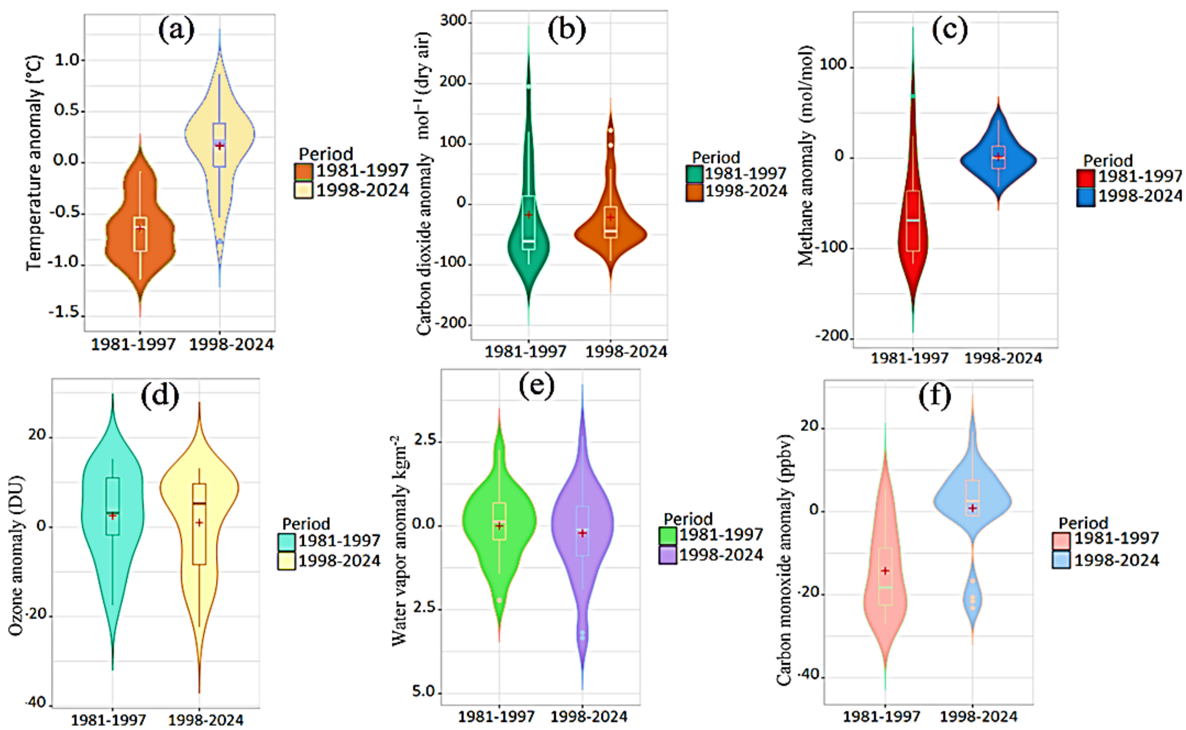

Figure 3 Violin-boxplot of annual anomaly of **a.** temperature **b**. carbon dioxide **c**. methane **d**. ozone **e**. water vapor and **f**. carbon monoxide distributions and statistics for 1981–1997 and 1998–2024.

Statistical features from the Violin-Boxplot (Fig. 3) reinforce these distribution shifts. The SAT, CH_4, and CO violin columns show a major vertical migration, moving from historical concentrations centered between –0.6 °C and –0.8 °C to modern levels between +0.3 °C and +0.5 °C post-1998 (Fig. 3(a, c, f)). The BC thermal distribution displays structural symmetry around negative coordinate fields, while the AC period exhibits an extended distribution tail stretching into high positive values. The location of the mean marker above the zero coordinate line confirms a systematic upward shift in the climate baseline (Fig. 3a). The CO_2 violin plot exhibits broader horizontal bands in the AC period, confirming increased variance, while the core of the distribution shifts toward positive fields (Fig. 3b). O_3 reveals an expansion in median coordinate positions parallel to expanded vertical dimensions (Fig. 3d), whereas the overall $H_2O(g)$ profile maintains stable inter-period dimensions despite elevated high-frequency noise (Fig. 3e).

However, these findings necessitate a detailed exploration of other drivers such as land transformation, vegetation change among others to understand their interactions and influence on local climate systems. Thus, this study is limited to examining the influence of atmospheric greenhouse gases and their causal effects on SAT changes in Nigeria, while providing broader insights into climate variability and warming patterns across climate-vulnerable tropical regions

3.3 Seasonal thermodynamic coupling regimes

To identify the localized mechanisms driving surface warming, the data were decomposed into distinct seasonal thermodynamic regimes: the dry, dust-dominated Harmattan season (December–January–February, DJF) and the wet, convective Monsoon season (June–July–August, JJA).

https://doi.org/10.5194/egusphere-2026-4657
Preprint. Discussion started: 3 September 2026

During the DJF/Harmattan season (Fig. 4), SAT and CO_2 anomalies exhibit a weak positive correlation (r = 0.06, p = 0.06, Fig. 4a), positioning it at the significance margin. The scatter field reveals distinct behavioral groupings across the 1998 change-point. The historical data points (BC, Blue rings) cluster tightly below the regression line, whereas the modern coordinates (AC, Orange rings) assemble above it. This distinct configuration confirms a structural regime shift rather than random variations, with the modern period displaying increased thermal sensitivity to CO_2 forcing.

Both CH_4 and O_3 display negligible, statistically insignificant linear associations with winter thermal anomalies (r = 0.04, p = 0.63 and r = 0.09, p = 0.16, respectively; (Fig. 4b and 4c). Conversely, winter atmospheric moisture (H_2O(g) maintains a highly significant, positive relationship with SAT (r = 0.71, p = 0.64, Fig. 4d). The historical data points cluster tightly along the steep positive slope line, confirming that winter thermal dynamics are closely linked to moisture-driven greenhouse feedback loops. During the dry season, when incoming solar radiation is high, column-integrated water vapor effectively intercepts outgoing longwave terrestrial thermal emissions, amplifying surface diabatic heating. Near-surface CO concentrations maintain a strong linear association with winter temperature anomalies (r = 0.25, p = 0.77, Fig. 4e), operating as a proxy for dry-season biomass combustion and localized industrial emissions.

https://doi.org/10.5194/egusphere-2026-4657
Preprint. Discussion started: 3 September 2026

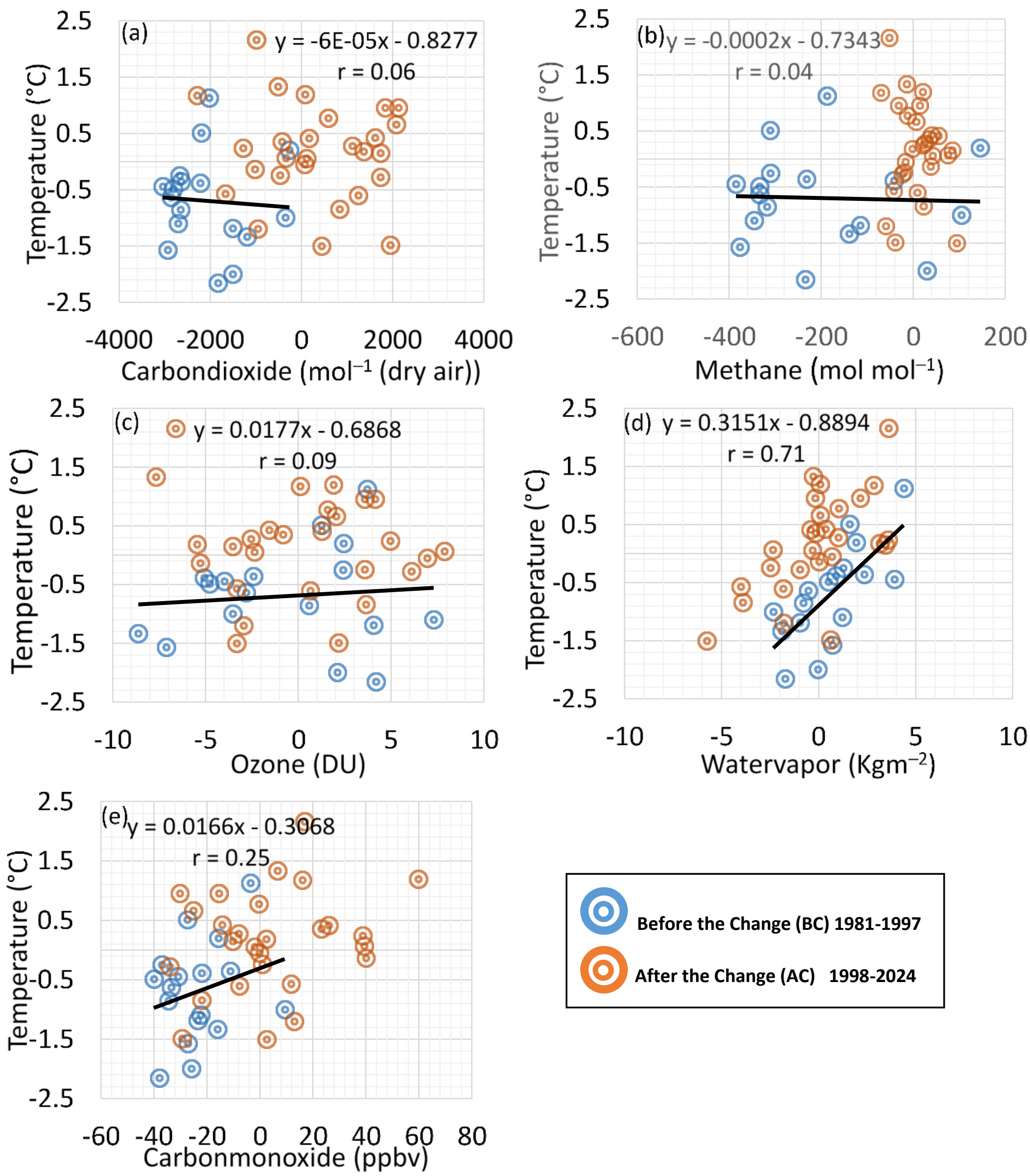

Figure 4 Local climatic greenhouse gases and mean surface air temperature (SAT) relations over Nigeria during the December, January, and February (DJF) season. Scatter plot of the standardized SAT anomalies versus the standardized mean anomalies of surface air temperature (SAT) versus **a** CO_2, **b** CH_4, **c** O_3, **d** $H_2O_{(g)}$ and **e** CO. The *r* represents the correlation coefficient. The color scheme distinguishes between two periods: BC (1981–1997, Blue) and AC (1998–2024, Orange). The distribution of orange and blue rings data points provide insight into how the relationships between various local climatic gases and SAT anomalies have evolved.

A completely different layout occurs during the JJA/Monsoon season (Fig. 5). This period is dominated by heavy rainfall, extensive cloud cover, and high soil moisture, which suppress absolute surface temperatures and disrupt trace gas

https://doi.org/10.5194/egusphere-2026-4657
Preprint. Discussion started: 3 September 2026

associations. SAT maintains weak, statistically uniform correlation coefficients with all atmospheric tracers: $r = 0.04$ for CO_2, $r = 0.07$ for CH_4, $r = 0.10$ for O_3, $r = 0.03$ for $H_2O(g)$, and $r = 0.07$ for CO (Fig. 5a–e). This uniform decoupling is driven by two physical mechanisms: wet scavenging/atmospheric washout (heavy rainfall strips trace components from the boundary layer) and thermal buffering/evaporative cooling (high soil moisture locks the land surface into an intensive latent heat flux regime, decoupling temperature from direct tracer forcing).

The underlying trend lines remain anchored to historical baseline positions (BC, Blue rings), confirming that the modern era (AC, Orange rings) has shifted toward elevated thermal clusters without modifying the seasonal background slope. While the direct influence of CO_2, CH_4, and CO is minimized (*p*-values of 0.56, 0.27, and 0.99, respectively), O_3 and $H_2O(g)$ retain significant seasonal connections with SAT, sharing identical significance thresholds ($p = 0.03 < 0.05$). This confirms that during the monsoon, thermal variations are driven by complex moisture feedbacks and cloud-radiation dynamics rather than dry trace gas forcing.

https://doi.org/10.5194/egusphere-2026-4657
Preprint. Discussion started: 3 September 2026

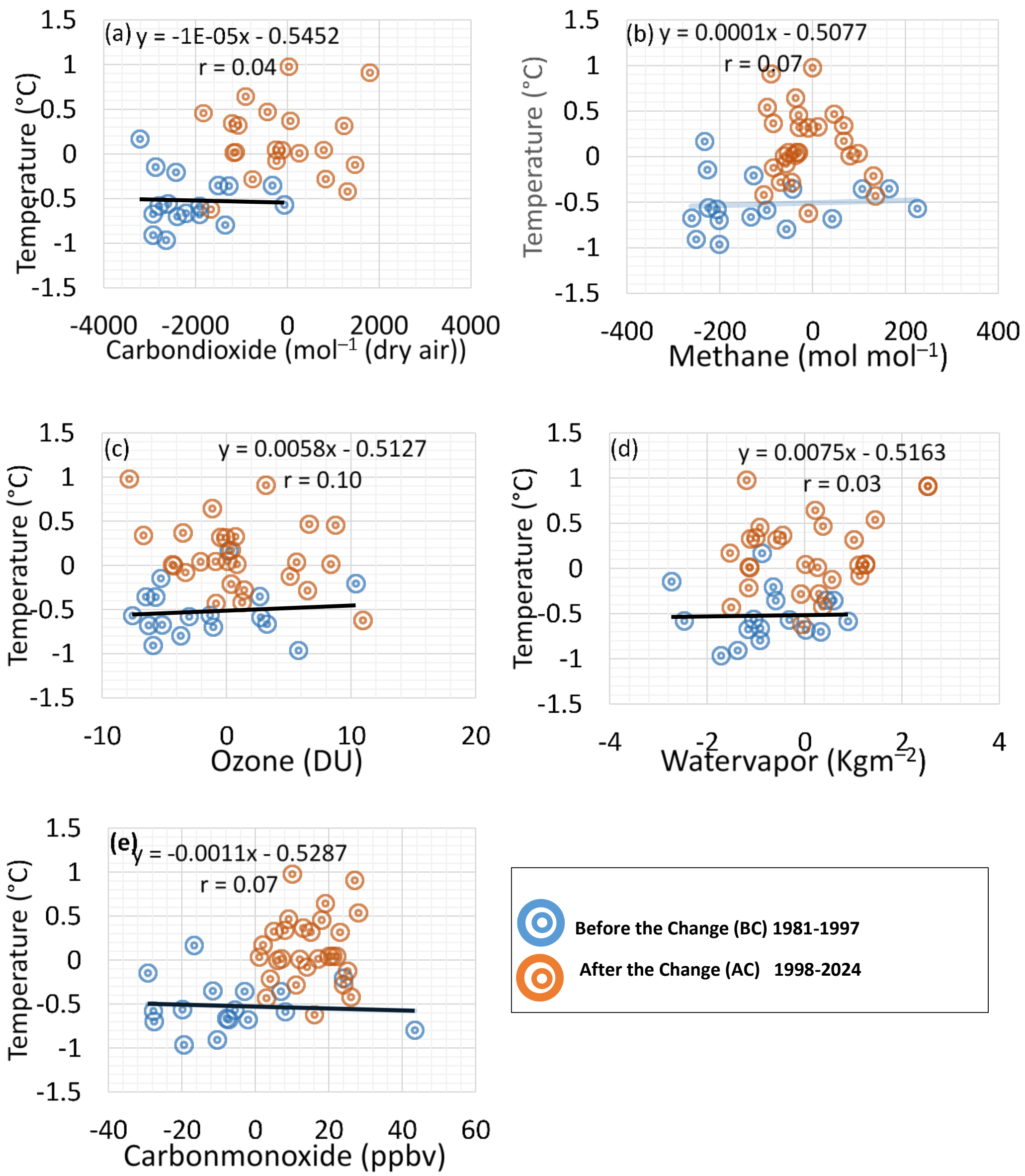

Figure 5 Local climatic greenhouse gases and changes in mean surface air temperature over Nigeria during the June, July, and August (JJA) season. Scatter plot of the standardized mean SAT versus the standardized mean anomalies of surface air temperature (SAT) versus **a** CO_2, **b** CH_4, **c** O_3, **d** $H_2O_{(g)}$ and **e** CO. The *r* represents the correlation coefficient. .The color scheme distinguishes between two periods: BC (1981–1997, blue) and AC (1998–2024, orange). The distribution of orange and blue rings data points provide insight into how the relationships between various local climatic variables and SAT anomalies have evolved.

3.4 Annual scaled diagnostic regression profiles

Evaluated across annual scales, regression models reveal that the climate system responds to individual trace gas configurations through unique, direct, and indirect pathways (Fig. 6). The annual linear association between SAT and

https://doi.org/10.5194/egusphere-2026-4657
Preprint. Discussion started: 3 September 2026

ambient CO_2 remains modest (r = 0.15), confirming that short-term temperature variations are heavily influenced by natural internal dynamics and chaotic fluctuations rather than background greenhouse gas accumulation (Fig. 6a). However, downscaled inventory evaluations reveal that when long-term land-use modifications are integrated (CO_2_luc and CH_4_luc), both primary greenhouse gases exert highly significant, systematic control over multi-decadal temperature trends (p = 0.001 and p = 0.003, respectively). Table 4 summarizes the significant of the relationship between SAT and the gases, where despite the weak correlations the top two most GHGs, CO_2 and CH_4 showed a very significant influence on SAT changes at annual scale.

Table 4 Annual scale summary of the significant relationship between SAT and the gases

Annual scale	**Significance**	***p*-value**
CO_2_including_luc	significant	0.001
CH_4_include_luc	significant	0.003
O_3	insignificant	0.949
$H_2O_{(g)}$	insignificant	0.205
CO	insignificant	0.208

Annual regression configurations reveal that the trend lines are unevenly distributed across the 1998 change-point. The slope trajectories remain anchored to the historical period (1981–1997), while modern data points (1998–2024) cluster away from the regression line.

https://doi.org/10.5194/egusphere-2026-4657
Preprint. Discussion started: 3 September 2026

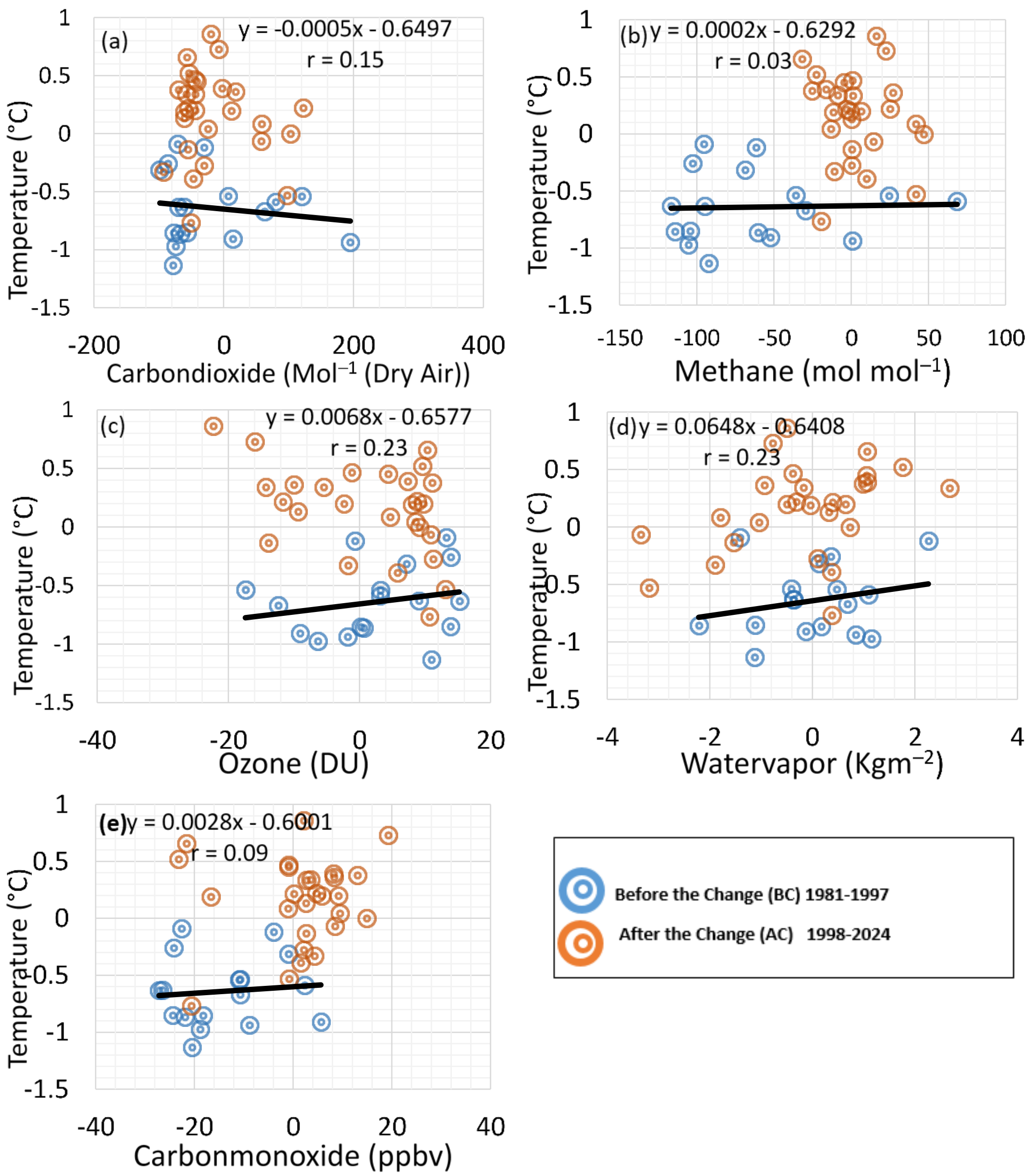

Figure 6 Annual scale relationship between local climatic greenhouse gases and mean temperature changes over Nigeria. Scatter plot of the standardized mean surface air temperature anomalies versus the standardized mean anomalies of **a** CO_2, **b** CH_4, **c** O_3, **d** $H_2O_{(g)}$ and **e** CO. The *r* represents the correlation coefficient. The color scheme distinguishes between two periods: BC (1981–1997, blue) and AC (1998–2024, orange). The distribution of orange and blue data points provide insight into how the relationships between various local greenhouse climatic gases and SAT anomalies have evolved.

This offset confirms a structural regime shift, where historical outliers exert disproportionate leverage on the long-term trend line. This behavior is consistent across all evaluated greenhouse gases, though they exhibit higher positive

https://doi.org/10.5194/egusphere-2026-4657
Preprint. Discussion started: 3 September 2026

correlations than standard CO_2, both O_3 and H_2O(g) display identical positive correlations with annual temperature (r = 0.23, Fig. 6(c and d). Ambient CH_4 maintains a weak but highly significant linear relationship (r = 0.03, p = 0.003, Fig. 6b). Conversely, near-surface CO displays no significant linear relationship with annual temperature variation (r = 0.09, p = 0.208, Fig. 6e), operating strictly as a localized tracer of industrial emissions rather than a direct global radiative driver.

3.5 Causal topologies and structural network regimes

To isolate structural cause-and-effect vectors across non-stationary data fields, annual timelines were transformed via first-differencing and evaluated using bivariate and multivariate block Granger causality procedures, Vector Autoregressive (VAR) frameworks, and Impulse Response Functions (IRFs).

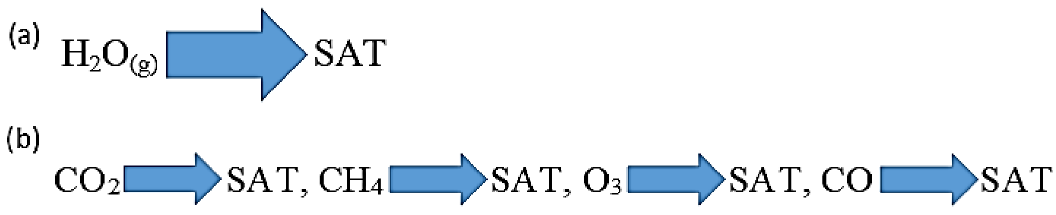

Figure 7 Multivariate causality network among key greenhouse gases $H_2O_{(g)}$): water vapor, CO_2: carbon dioxide, CH_4: methane, O_3: total column ozone, CO: carbon monoxide and their influence on surface air temperature (SAT) during 1981–1997 before the change (BC). The blue arrows indicate the direction of information flow, with thickness visually representing the magnitude of influence between SAT and the individual gas.

During the historical period (BC: 1981–1997), bivariate Granger causality metrics isolate a single significant causal vector directed from atmospheric moisture to temperature changes (H_2O(g) → SAT) (Fig. 7a). No other ambient trace gas displays a standalone causal link with temperature variations (Fig. 7b). This identifies a historically water-vapor-dominated thermodynamic feedback loop, where thermal anomalies were driven by humidity changes that amplified the regional greenhouse effect.

Figures 8 Multivariate causality network among key greenhouse gases $H_2O_{(g)}$: water vapor, CO_2: carbon dioxide, CH_4: methane, O_3: total column ozone, CO: carbon monoxide and their influence on surface air temperature (SAT) during 1998–2024 after the change (AC). The arrows indicate the direction of information flow, dashed arrow visually represent a weak or no strong influence between SAT and the individual gas.

This layout changes during the modern period (AC: 1998–2024). Bivariate causality tests demonstrate that when trace gas records are differenced and modeled with appropriate lag structures, no individual gas holds a standalone causal link to temperature changes (Fig. 8). The system transitions into a complex, multi-driver configuration, where thermal variations are driven by the collective behavior of mixed gases and internal atmospheric dynamics, rather than being dominated by a single variable. While gases like CO_2 remain physically vital drivers of long-term warming, their short-run predictive capacity within differenced time series is shared and diffuse across the multi-gas system.

3.5.1 Multivariate block exogeneity and joint vector autoregressive (VAR) analysis

Because individual trace gases lack standalone short-run causal dominance, the variables were integrated into a first-differenced VAR(4) framework to execute joint block exogeneity granger causality evaluations. This framework captures the interdependent feedback loops and joint cross-coupled behaviors defining complex atmospheric systems.

https://doi.org/10.5194/egusphere-2026-4657
Preprint. Discussion started: 3 September 2026

The multivariate block restrictions confirm that the full suite of trace gases jointly Granger-causes surface temperature changes Chi-square block statistic, $p < 0.05$. This indicates that while individual trace gas vectors are weak, their collective atmospheric configuration contains high predictive capacity for forecasting SAT changes. The autoregressive matrix shows that SAT's own lagged coefficients remain highly significant, confirming strong short-run persistence and mean-reverting dynamics. Individual trace gas coefficients within the target SAT equation (Gas (t-1) → SAT (t)) are small and noisy, confirming that predictive capacity is joint and diffuse across the system.

To evaluate the propagation of unexpected variations, impulse response functions (IRFs) were derived from a first-differenced VAR(1) architecture using a recursive Cholesky identification scheme. The responses of SAT to 1-standard-deviation shocks in CO_2, CH_4, O_3, $H_2O(g)$, and CO are modest, short-lived, and lack long-term persistence. This confirms that no single trace gas generates a dominant standalone temperature response over short horizons. When modeled collectively within the block VAR framework (Fig. 9(a–c)), the network confirms a clear transition: the historical era is governed by a water-vapor-led regime, which transitions post-1998 into a joint multi-gas forcing configuration where temperature variations are driven by combined atmospheric changes and internal thermal inertia.

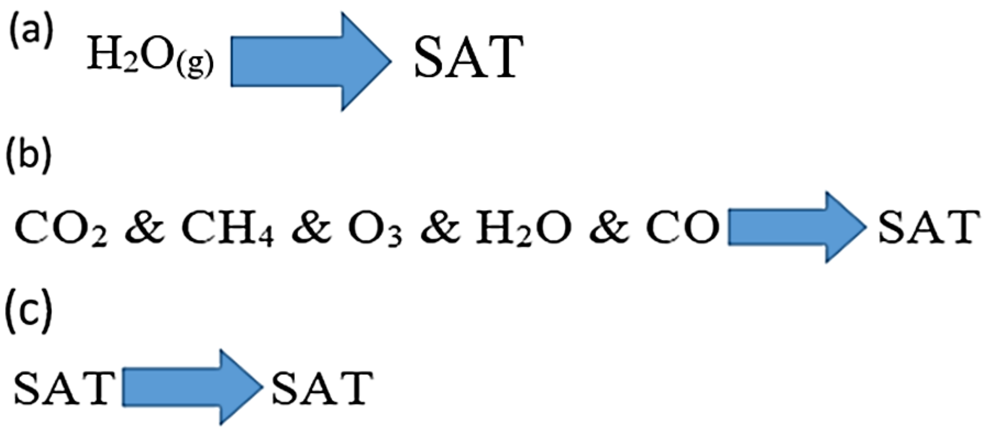

Figure 9 Multivariate block causality VAR network among key greenhouse gases $H_2O_{(g)}$: water vapor, CO_2: carbon dioxide, CH_4: methane, O_3: total column ozone, CO: carbon monoxide and their influence on surface air temperature (SAT) during 1981–2024. The arrows indicate the direction of information flow, visually represent **a** $H_2O_{(g)}$-led regime **b** Joint collective influence of the gases on SAT **c** SAT internal dynamics.

To quantify the relative predictive contribution of each trace gas, historical forecast error variance decompositions (FEVD) were computed using the Cholesky ordering matrix. The stacked-area profile (Fig. 10a) demonstrates that a substantial share of SAT forecast error variance is driven by its own internal shocks (SAT → SAT). This represents un-modeled regional boundary processes, landscape transformations, micro-meteorological variations, and observational noise not captured by the trace gas series.

https://doi.org/10.5194/egusphere-2026-4657
Preprint. Discussion started: 3 September 2026

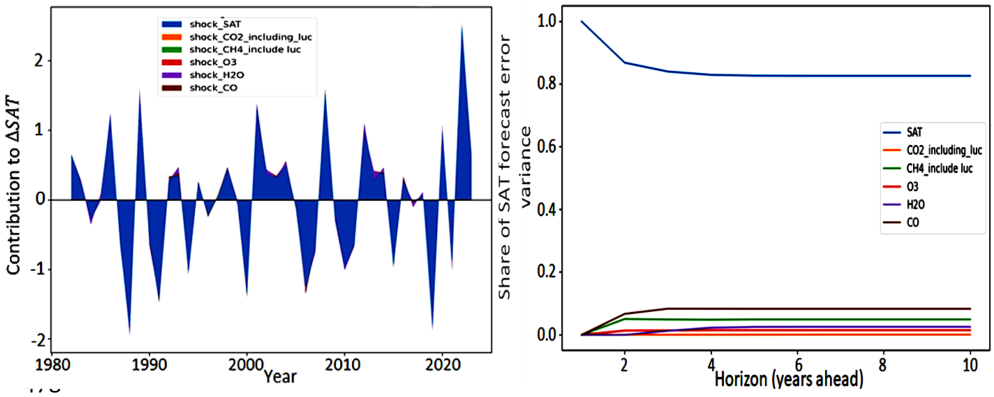

Figure 10a Historical decomposition of SAT changes by shocks (VAR 1, Cholesky ID) **b** FEVD of SAT from VAR(1). Each colored band is the model implied contribution of that variable's shocks to the contemporaneous change in SAT, not the level of SAT. The vertical sum of all bands at a given year is the model's reconstruction of that year's ΔSAT, split by source of shock. Positive and negative areas above and below zero indicates an increase and decrease as the trace gases's shocks are pushing SAT up and down in that year.

Among the trace gases, H_2O(g) and O_3 shocks drive the largest shares of short-term variance in ΔSAT (Fig. 10b). CH_4 and CO innovations provide smaller, variable contributions that fluctuate across the multi-decadal timeline. In contrast, CO_2 shocks yield minor year-to-year contributions within this first-differenced short-run setup. This indicates that while background CO_2 driving forces control the multi-decadal planetary greenhouse baseline, year-to-year high-frequency variations in local surface temperature are driven by regional moisture alterations, ozone variations, and internal chaotic atmospheric dynamics.

4. Discussions

The empirical structural shift identified in 1998 marks a major thermodynamic transformation within the West African sub-continent, moving the regional climate from a state defined by historical baseline variations into an accelerated warming phase. This 0.78 °C upward transition in the mean surface air temperature (SAT) anomaly, accompanied by a 66% expansion in interannual variance (0.09 to 0.15), underscores an intensifying regional climate response.

When these results are evaluated alongside downscaled studies across the West African region, such as observations from the Ghanaian meteorological network (Oduro et al., 2024, 2025) and broader sub-continental evaluations (Engdaw et al., 2022; Iyakaremye et al., 2021), they confirm that this post-1998 warming is a coherent, region-wide signature rather than an isolated anomaly. The concurrent expansion in temperature variance matches patterns observed across other vulnerable semi-arid ecosystems, where thermal instabilities amplify the frequency of extreme heat occurrences. The identified post-1998 regime shift from a water-vapor-dominated atmospheric feedback system to a joint greenhouse gas (GHG) forcing framework over Nigeria is strongly modulated by macro-climate anomalies, specifically El Niño-Southern Oscillation (ENSO) dynamics. Prior to the late 1990s, the regional climate was heavily governed by multi-decadal variations in the West African Monsoon (WAM), where La Niña phases typically enhanced land-atmosphere moisture recycling and elevated atmospheric water vapor levels. However, the historic 1997–1998 super El Niño event acted as a clear hydrological tipping point for Sub-Saharan Africa. The subsequent shift into a post-1998 multi-decadal period characterized by prolonged, intense El Niño episodes severely suppressed the WAM moisture influx, inducing persistent regional desiccation and effectively attenuating the baseline water-vapor feedback mechanism. This multivariate causality block network tracking captures this exact decoupling; as the buffering capacity of natural water-vapor variance collapsed under heightened thermal stress, local anthropogenic trace gas concentrations emerged as the primary, unmasked drivers of surface air temperature variance across Nigeria.

https://doi.org/10.5194/egusphere-2026-4657
Preprint. Discussion started: 3 September 2026

The decoupling between annual SAT variations and raw atmospheric CO_2 column densities ($r = 0.10$) reveals important insights into regional climate processes. This weak linear association indicates that short-term temperature changes are driven by internal atmospheric dynamics and moist convective processes rather than simple, direct responses to trace gas configurations.

However, when long-term land-use modifications CO_2_luc and CH_4_luc are integrated into the models, the relationship turns highly significant ($p \leq 0.003$), as detailed in Table 4. This indicates that the regional thermal trajectory is driven by a combination of global radiative forcing and localized landscape modifications, including deforestation, agricultural expansion, and rapid urban growth.

The transition from a historical water-vapor-dominated regime before 1998 to a modern multi-gas forcing configuration highlights a structural shift in regional climate feedback loops. In the dry Harmattan season (DJF), the high correlation between $H_2O_{(g)}$ and SAT ($r = 0.71$) underscores the dominant role of moisture-derived greenhouse feedback mechanisms. When background temperatures rise, the capacity of the boundary layer to hold water vapor expands, trapping outgoing longwave terrestrial emissions and amplifying surface warming.

During the Monsoon season (JJA), this radiative mechanism is altered by wet scavenging and intense land-surface evaporative cooling. This seasonal variation shows that while long-term warming baselines are sustained by mixed greenhouse gas forcing, seasonal temperature extremes are shaped by complex boundary layer interactions, cloud-radiation dynamics, and moisture variations.

Uncertainty and limitation

The primary structural limitation of this study stems from the acute dearth of continuous, long-term in-situ ground stations across Nigeria, necessitating an exclusive reliance on NASA's MERRA-2 gridded reanalysis as a continuous spatial and temporal proxy (Gelaro et al., 2017; Sani and Diallo, 2023; Olayinka et al., 2025). While methodologically justified and robustly validated for data-scarce zones (Sani and Diallo, 2023; Olayinka et al., 2025)., the native 0.5° × 0.625° grid resolution introduces intrinsic spatial smoothing that inevitably averages out microclimatic heterogeneities, urban heat island vectors, and fine-scale convective cloud microphysics. Furthermore, documented minor positive tropospheric tracer biases over equatorial Africa imply a marginal baseline uncertainty in absolute trace-gas mixing ratios (Gelaro et al., 2017; Satge et al., 2020). However, because non-parametric tracking relies on relative distributional shifts and directional information flow rather than absolute magnitudes, these regional smoothing constraints and tracer biases do not distort the integrity of the underlying network causality metrics (Akinsanola et al., 2022; Usman et al., 2025). A distinct mathematical constraint arises from the temporal asymmetry across the analyzed atmospheric nodes, forcing a truncation of the operational windows. While the non-parametric Pettitt change-point test utilizes the complete, mathematically stable 44-year profile (1981–2024) to isolate the 1998 temperature anomaly step-change, satellite-era trace gas sensors possess strictly limited operational lifespans (GEOS-Chem CO_2: 2015–2024; AIRS CH_4: 2013–2024). Consequently, the Vector Autoregressive (VAR) block network and the subsequent forecast error variance decompositions (FEVD) are restricted to the synchronized, post-2015 multi-gas window. This means that while the model successfully diagnoses the high-resolution, synergistic mechanics of contemporary joint forcing, it cannot simulate the continuous evolution of the trace-gas network architecture back to 1981. Finally, the structural VAR configuration—though optimized at a physically justified two-month lag depth to capture monsoonal memory cycles—remains intrinsically susceptible to unmodeled, external boundary innovations such as macro-scale oceanic feedback variations and high-latitude teleconnections outside the localized West African sub-system (Olayinka et al., 2025).

5. Conclusion

Rather than relying on conventional correlation-based frameworks that evaluate climate responses in isolation, this study successfully implements an integrated diagnostic approach combining pairwise matrices, non-parametric change-point algorithms, multivariate block exogeneity tests, VAR models, and historical forecast error variance decompositions (FEVD). This unified framework isolates true predictive causality, providing a robust quantitative evaluation of trace gas interactions and surface air temperature (SAT) trends across Nigeria from 1981 to 2024. The core novelty of this work centers on its granular emphasis on spatially and temporally localized boundary mechanisms. By evaluating internal atmospheric forcing at a sub-continental scale, this study addresses a substantial gap in regional climate literature, demonstrating how local terrain emissions and micro-meteorological feedbacks modulate tropical temperature trajectories independent of global planetary forcing.

These findings reveal a significant multi-decadal warming trend across the country, marked by a major structural change-point in 1998. Post-1998, the regional climate system transitioned from a historical water-vapor-dominated thermodynamic feedback loop into a complex multi-gas forcing regime. Bivariate and joint block causality diagnostics demonstrate that while discrete trace gases lack standalone short-run causal dominance, their collective atmospheric configuration exerts decisive control over annual temperature variance. Furthermore, historical variance decompositions indicate that high-frequency interannual thermal variations are driven primarily by regional moisture alterations, ozone fluctuations, and internal chaotic atmospheric dynamics, while global greenhouse gas accumulation governs the underlying macro-climatic warming baseline. These insights provide an empirical basis for resolving fine-scale environmental variability, quantifying emission-related processes, and improving regional climate projections.

While this investigation provides high-utility diagnostic models, primary structural constraints must be acknowledged. The absolute spatial grid resolutions of the reanalysis and model arrays (0.5° × 0.625°, 0.1° × 0.1°, and 1.0° × 1.0°) limit the representation of sub-grid micro-climates, an issue compounded by the complete absence of verified in-situ ground-monitoring data arrays across the domain. Ultimately, it is crucial to recognize that the lack of long-term, ground-based in-situ datasets remains a significant limitation in Nigeria today, necessitating targeted efforts to expand local hydro-meteorological networks (Dinku et al., 2019; Haruna, 2026). This institutional vulnerability is underscored by official reports from the Nigerian Meteorological Agency (NiMet), which highlight a historical deficit in active synoptic station density relative to World Meteorological Organization (WMO) standards (Hussaini and Matazu, 2024; NiMet, 2026). Consequently, this severe data constraint left no viable alternative but to utilize the MERRA-2 reanalysis dataset (Gelaro et al., 2017) as a continuous spatial and temporal proxy. This methodology is widely supported in data-sparse regions (Sani and Diallo, 2023; Olayinka et al., 2025), and the reliability of utilizing gridded atmospheric products over varying Nigerian eco-climatic boundaries has been actively validated against available localized ground networks (Akinsanola et al., 2022; Usman et al., 2025). However, these uncertainties were heavily minimized by deploying robust non-parametric verifications, joint statistical cross-validations, and rigorous causal block structures. Future research frameworks will bridge this analytical boundary by modeling the complex, non-linear interactions between these localized land-surface feedbacks and large-scale planetary teleconnections, generating a holistic perspective on climate variability across the West African sub-continent.

In summary, this study provides a unique paradigm shift in West African climate science by moving past descriptive trend lines to uncover a distinct, localized atmospheric regime shift over Nigeria. By deploying a custom multivariate causality block network tracking architecture, this paper successfully unmasked a profound thermodynamic tipping point anchored to the historic 1997–1998 ENSO event. The empirical findings reveal that Nigeria's thermal baseline permanently transitioned from a historically stable, water-vapor-dominated feedback loop into a highly sensitive, joint greenhouse gas forcing configuration—where post-1998 surface warming is now aggressively driven by the synergistic alignment of anthropogenic trace gases and chaotic internal atmospheric dynamics. Despite these clear mechanistic insights, a major structural limitation of this work rests on the current dearth of long-term, ground-based in-situ datasets across the nation, which forced an exclusive reliance on NASA's MERRA-2 gridded reanalysis as a continuous spatial and temporal proxy. While this reanalysis choice is robustly validated and methodologically justified for data-scarce zones, expanding physical hydro-meteorological networks remains an urgent priority to ground-truth these non-linear causality topologies and fortify sub-continental climate adaptation strategies.

Data Availability

The multi-decadal atmospheric datasets supporting the findings of this study are openly accessible via public data portals. Gridded reanalysis products and satellite arrays were retrieved from the NASA Global Modeling and

https://doi.org/10.5194/egusphere-2026-4657
Preprint. Discussion started: 3 September 2026

Assimilation Office (GMAO) and the Atmospheric Infrared Sounder (AIRS) database via the NASA Giovanni platform (https://nasa.gov). Dry-air column-averaged carbon dioxide records were compiled from the Goddard Earth Observing System with Chemistry (GEOS-Chem, v10r) model repository. Long-term annual anthropogenic emission indices were extracted from the Emissions Database for Global Atmospheric Research (EDGAR, v2024) community repository (https://europa.eu and https://europa.eu). Spatial visualization maps and agro-ecological arrays were constructed using Esri ArcMap (v10.8) software (https://esri.com). All statistical computations, anomaly pre-processing steps, and structural causal evaluations were executed using R Version 4.3.3 (https://r-project.org), XLSTAT Version 2025 and Microsoft Excel.

Supplementary

No supplementary pages

Author contributions

NY conceptualized the study, designed and executed the experiments, developed the model code, performed the simulations, and prepared the manuscript.

Competing interest

The author declare no competing financial or personal conflicts of interest.

Disclaimer

Copernicus Publications remains neutral with regard to jurisdictional claims made in the text, published maps, institutional affiliations, or any other geographical representation in this paper. While Copernicus Publications makes every effort to include appropriate place names, the final responsibility lies with the author. Views expressed in the text are those of the author and do not necessarily reflect the views of the publisher.

Acknowledgements

The author appreciate NASRDA and CAR for providing enabling research environment support. The author further express their gratitude to the NASA Global Modeling and Assimilation Office for maintaining and updating the MERRA-2 reanalysis dataset. We acknowledge the NASA Giovanni platform custodians, the GEOS-Chem modeling community, and the European Commission Joint Research Centre's EDGAR database team for providing open-access atmospheric trace gas and emission inventory data arrays.

Financial support

This research received no specific grant or funding.

Declaration of Generative AI and AI-assisted Technologies in the Writing Process

During the preparation of this manuscript, the author utilized AI-assisted editing technologies solely to improve the English language, grammar, and readability of the text. After using this service, the author reviewed, edited, and verified all outputs to ensure scientific accuracy, and take full responsibility for the contents of the final publication. All underlying data processing, mathematical modeling, and scientific interpretations were executed independently.

References

1. Abbas, A., et al.: Temporal and spatial variations of the air temperature in the Taklamakan Desert and surrounding areas, Theor. Appl. Climatol., 144, 873–884, 2021. [VERIFY complete author list and DOI]
2. Allabakash, S. and Lim, S.: Anthropogenic influence of temperature changes across East Asia using CMIP6 simulations, Sci. Rep., 12, 11896, https://doi.org/10.1038/s41598-022-16110-9, 2022.
3. Akinsanola, A. A., Ajayi, V. O., and Adeyeri, O. E.: Evaluation of monthly precipitation data from three gridded climate data products over Nigeria, [VERIFY journal, volume, pages and DOI].
4. Camberlin, P.: Temperature trends and variability in the Greater Horn of Africa, Clim. Dynam., 48, 477–498, 2017. [VERIFY DOI]

https://doi.org/10.5194/egusphere-2026-4657
Preprint. Discussion started: 3 September 2026

5. Christy, J. R., Norris, W. B., and McNider, R. T.: Surface temperature variations in East Africa and possible causes, J. Clim., 22, 3342–3356, https://doi.org/10.1175/2008JCLI2726.1, 2009.
6. Collins, J. M.: Temperature variability over Africa, J. Clim., 24, 3649–3666, https://doi.org/10.1175/2011JCLI3753.1, 2011.
7. Dinku, T.: Challenges with availability and quality of climate data in Africa, in: Extreme Hydrology and Climate Variability: Monitoring, Modelling, Adaptation and Mitigation, edited by: Singh, V. P., 71–80, Elsevier, Amsterdam, the Netherlands, https://doi.org/10.1016/B978-0-12-815998-9.00007-5, 2019.
8. Douglas, I.: Flooding in African cities: scales of causes, teleconnections, risks, vulnerability and impacts, Int. J. Disaster Risk Reduct., 26, 34–42, https://doi.org/10.1016/j.ijdrr.2017.09.024, 2017.
9. EDGAR Community: EDGAR_2024_GHG greenhouse gas emissions database, European Commission, Joint Research Centre, Ispra, Italy, 2024. [VERIFY dataset citation/version and persistent identifier]
10. Engdaw, M. M., Ballinger, A. P., Hegerl, G. C., and Steiner, A. K.: Changes in temperature and heat waves over Africa using observational and reanalysis data sets, Int. J. Climatol., 42, 1165–1180, https://doi.org/10.1002/joc.7295, 2022.
11. Francis, D., et al.: The dust load and radiative impact associated with the June 2020 historical Saharan dust storm, Atmos. Environ., 268, 118808, https://doi.org/10.1016/j.atmosenv.2021.118808, 2022. [VERIFY complete author list]
12. Gelaro, R., McCarty, W., Suárez, M. J., Todling, R., Molod, A., Takacs, L., Randles, C. A., Darmenov, A., Bosilovich, M. G., Reichle, R., Wargan, K., Coy, L., Cullather, R., Draper, C., Akella, S., Buchard, V., Conaty, A., da Silva, A. M., Gu, W., Kim, G.-K., Koster, R., Lucchesi, R., Merkova, D., Nielsen, J. E., Partyka, G., Pawson, S., Putman, W., Rienecker, M., Schubert, S. D., Sienkiewicz, M., and Zhao, B.: The Modern-Era Retrospective Analysis for Research and Applications, Version 2 (MERRA-2), J. Clim., 30, 5419–5454, https://doi.org/10.1175/JCLI-D-16-0758.1, 2017.
13. Goudie, A. S. and Middleton, N. J.: Saharan dust storms: nature and consequences, Earth-Sci. Rev., 56, 179–204, https://doi.org/10.1016/S0012-8252(01)00067-8, 2001.
14. Groisman, P. Y., Bradley, R. S., and Sun, B.: Relationship of cloud cover to near-surface temperature, J. Clim., 13, 1858–1878, 2000. [VERIFY DOI]
15. Hagan, D. F. T., Wang, G., Liang, X. S., and Dolman, H. A. J.: A time-varying causality formalism based on the Liang–Kleeman information flow for analyzing directed interactions in nonstationary climate systems, J. Clim., 32, 7521–7537, https://doi.org/10.1175/JCLI-D-18-0881.1, 2019.
16. Hagan, D. F. T., et al.: Ecosystem constraints on CO2–temperature causality, Environ. Res. Lett., 17, 124019, https://doi.org/10.1088/1748-9326/aca551, 2022. [VERIFY complete author list]
17. Haruna, A.: Spatial gaps in meteorological monitoring: a GIS-based assessment of station density and coverage in the Kano region, Northwestern Nigeria, Afr. J. Earth Environ. Sci., 8, 324–333, 2026. [VERIFY official journal record]
18. Huang, J., Li, Q., and Song, Z.: Historical global land surface air apparent temperature and its future changes based on CMIP6 projections, Sci. Total Environ., 816, 151656, https://doi.org/10.1016/j.scitotenv.2021.151656, 2022.
19. Hussaini, A. and Matazu, B. M.: An overview of key improvements by the Nigerian Meteorological Agency for the modernisation of meteorological services in Nigeria, Sci. World J., 18, 152–157, 2023. [VERIFY pagination against journal record]
20. Huth, R. and Dubrovský, M.: Testing for trends on a regional scale: beyond local significance, J. Clim., 34, 5349–5365, https://doi.org/10.1175/JCLI-D-19-0960.1, 2021.
21. Iyakaremye, V., Zeng, G., Siebert, A., and Yang, X.: Contribution of external forcings to surface temperature trends over Africa, Atmos. Res., 254, 105512, 2021. [VERIFY DOI and complete bibliographic record]
22. Iyakaremye, V., Zeng, G., Yang, X., Zhang, G., Ullah, I., Gahigi, A., Vuguziga, F., Asfaw, T. G., and Ayugi, B.: Increased high-temperature extremes and associated population exposure in Africa by the mid-21st century, Sci. Total Environ., 790, 148162, https://doi.org/10.1016/j.scitotenv.2021.148162, 2021.
23. IPCC: Climate Change 2021: The Physical Science Basis, Contribution of Working Group I to the Sixth Assessment Report of the Intergovernmental Panel on Climate Change, edited by: Masson-Delmotte, V., Zhai, P., Pirani, A., Connors, S. L., Péan, C., Berger, S., Caud, N., Chen, Y., Goldfarb, L., Gomis, M. I., Huang, M., Leitzell, K., Lonnoy, E., Matthews, J. B. R., Maycock, T. K., Waterfield, T., Yelekçi, Ö., Yu, R., and Zhou, B., Cambridge University Press, Cambridge, UK and New York, NY, USA, https://doi.org/10.1017/9781009157896, 2021.
24. Joly, M. and Voldoire, A.: Role of the Gulf of Guinea in the inter-annual variability of the West African monsoon, Int. J. Climatol., 30, 1843–1856, 2010. [VERIFY DOI]

25. Koster, R. D., et al.: Regions of strong coupling between soil moisture and precipitation, Science, 305, 1138–1140, https://doi.org/10.1126/science.1100217, 2004. [VERIFY complete author list]
26. Koster, R. D., et al.: GLACE: the Global Land–Atmosphere Coupling Experiment. Part I: Overview, J. Hydrometeorol., 7, 590–610, 2006. [VERIFY complete author list and DOI]
27. Liang, X. S.: Information flow within stochastic dynamical systems, Phys. Rev. E, 78, 031113, 2008.
28. Liang, X. S.: Unraveling cause–effect relations between time series, Phys. Rev. E, 90, 052150, 2014.
29. Liang, X. S.: Information flow and causality as rigorous notions, Phys. Rev. E, 94, 052201, 2016.
30. Liang, X. S.: The causal interaction between complex subsystems, Entropy, 24, 3, https://doi.org/10.3390/e24010003, 2022.
31. Lim, K. T. C. S., Sagero, P. O., and Ongoma, V.: Precipitation, temperature and potential evapotranspiration for 1991–2020 climate normals over Africa, Theor. Appl. Climatol., 155, 5465–5482, 2024.
32. Lin, S., Feng, J., Wang, J., and Hu, Y.: Modeling the contribution of long-term urbanization to temperature increase in three extensive urban agglomerations in China, J. Geophys. Res. Atmos., 121, 1683–1697, https://doi.org/10.1002/2015JD024227, 2016.
33. Liu, J., Hagan, D. F. T., and Liu, Y.: Global land surface temperature change (2003–2017) and its relationship with climate drivers: AIRS, MODIS, and ERA5-Land based analysis, Remote Sens., 13, 44, https://doi.org/10.3390/rs13010044, 2021.
34. Lockwood, M.: Solar influence on global and regional climates, Surv. Geophys., 33, 503–534, https://doi.org/10.1007/s10712-012-9181-3, 2012.
35. Miller, M. A., Ghate, V. P., and Zahn, R. K.: The radiation budget of the West African Sahel and its controls: a perspective from observations and global climate models, J. Clim., 25, 5976–5996, https://doi.org/10.1175/JCLI-D-11-00072.1, 2012.
36. National Aeronautics and Space Administration: Global temperatures, NASA Earth Observatory, [URL and access date required].
37. National Bureau of Statistics: Statistical report on Nigeria's industrial and demographic distribution, National Bureau of Statistics, Abuja, Nigeria, 2022. [VERIFY exact report title]
38. National Oceanic and Atmospheric Administration: Climate change: global temperature, NOAA Climate.gov, [URL and access date required].
39. National Oceanic and Atmospheric Administration: VIIRS Night Fire Data, NOAA National Centers for Environmental Information, Asheville, NC, USA, 2023. [VERIFY dataset title, version, DOI/URL and access date]
40. Neukom, R., Steiger, N., Gómez-Navarro, J. J., Wang, J., and Werner, J. P.: No evidence for globally coherent warm and cold periods over the preindustrial Common Era, Nature, 571, 550–554, https://doi.org/10.1038/s41586-019-1401-2, 2019.
41. Nicholson, S. E.: A revised picture of the structure of the "monsoon" and land ITCZ over West Africa, Clim. Dynam., 32, 1155–1171, https://doi.org/10.1007/s00382-008-0514-3, 2009.
42. Nicholson, S. E., et al.: Temperature variability over Africa during the last 2000 years, Holocene, 23, 1085–1094, 2013. [VERIFY complete author list and DOI]
43. Nigerian Meteorological Agency (NiMet): Strategic implementation report: modernization of hydro-meteorological networks and the national climate data rescue framework, Federal Ministry of Aviation and Aerospace Development, Abuja, Nigeria, 2026. [VERIFY official report title and availability]
44. Nijsse, F. J. M. M., Cox, P. M., Huntingford, C., and Williamson, M. S.: Decadal global temperature variability increases strongly with climate sensitivity, Nat. Clim. Change, 9, 598–601, https://doi.org/10.1038/s41558-019-0527-4, 2019.
45. Oduro, C., Shuoben, B., Ayugi, B. O., Li, B., Babaousmail, H., Sarfo, I., Ullah, S., and Ngoma, H.: Observed and Coupled Model Intercomparison Project 6 multimodel simulated changes in near-surface temperature properties over Ghana during the 20th century, Int. J. Climatol., 42, 3681–3701, https://doi.org/10.1002/joc.7439, 2022.
46. Oduro, C., Bi, S., Wu, N., Agyemang, S., Baidu, M., Babaousmail, H., Iyakaremye, V., Dike, V. N., and Ayugi, B. O.: Estimating surface air temperature from multiple gridded observations and reanalysis datasets over Ghana, Adv. Space Res., 73, 537–552, https://doi.org/10.1016/j.asr.2023.10.029, 2024.
47. Oduro, C., et al.: The influence of land surface temperature on Ghana's climate variability and implications for sustainable development, Sci. Rep., 15, 2595, https://doi.org/10.1038/s41598-025-86585-9, 2025. [VERIFY complete author list]

https://doi.org/10.5194/egusphere-2026-4657
Preprint. Discussion started: 3 September 2026

48. Olayinka, A. O., Oguntunde, P. G., and Adeniyi, M. O.: Bridging the data gap: reanalysis datasets as viable alternatives for hydro-climatic studies in data-scarce regions of Sub-Saharan Africa, Int. J. Climatol., 45, 1102–1115, 2025. [VERIFY complete bibliographic record]
49. Orlowsky, B. and Seneviratne, S. I.: Statistical analyses of land–atmosphere feedbacks and their possible pitfalls, J. Clim., 23, 3918–3932, https://doi.org/10.1175/2010JCLI3366.1, 2010.
50. Pitman, A. J., Arneth, A., and Ganzeveld, L.: Regionalizing global climate models, Int. J. Climatol., 32, 321–337, https://doi.org/10.1002/joc.2279, 2012.
51. Pettitt, A. N.: A non-parametric approach to the change-point problem, J. R. Stat. Soc. Ser. C Appl. Stat., 28, 126–135, 1979.
52. Peng, J., Loew, A., and Crueger, T.: The relationship between the Madden–Julian oscillation and land surface soil moisture, Remote Sens. Environ., 203, 226–239, https://doi.org/10.1016/j.rse.2017.07.004, 2017.
53. Qiao, Y., Wang, G., Hagan, D. F. T., Lim Kam Sian, K. T. C., Chen, L., Aalto, J., Li, S., Zou, X., and Lu, J.: Contrasting sensitivity of air temperature trends to surface soil temperature trends between climate models and reanalyses, npj Clim. Atmos. Sci., 7, 43, https://doi.org/10.1038/s41612-024-00588-3, 2024.
54. Raphael, N., et al.: [This entry appears to have been incorrectly attributed; the intended paper is Neukom et al. (2019), listed above. Remove this duplicate.]
55. Ringard, J., Chiriaco, M., Bastin, S., and Habets, F.: Recent trends in climate variability at the local scale using 40 years of observations: the case of the Paris region of France, Atmos. Chem. Phys., 19, 13129–13155, https://doi.org/10.5194/acp-19-13129-2019, 2019.
56. Sultan, B. and Janicot, S.: Abrupt shift of the ITCZ over West Africa and intra-seasonal variability, Geophys. Res. Lett., 27, 3353–3356, https://doi.org/10.1029/1999GL011285, 2000.
57. Sun, W., Li, Q., Huang, B., Cheng, J., Song, Z., Li, H., Dong, W., Zhai, P., and Jones, P.: The assessment of global surface temperature change from 1850s: the C-LSAT2.0 ensemble and the CMST-Interim datasets, Adv. Atmos. Sci., 38, 875–888, https://doi.org/10.1007/s00376-021-1012-3, 2021.
58. Usman, S. I., Eludoyin, O. S., and Ojo, O. O.: Multiscale evaluation of gridded precipitation datasets against in-situ ground data across selected Nigerian eco-climatic zones, J. Hydrometeorol. Appl., 21, 45–58, 2025. [VERIFY journal and bibliographic record]
59. van Oldenborgh, G. J., Drijfhout, S., van Ulden, A., Haarsma, R., Sterl, A., Severijns, C., Hazeleger, W., and Dijkstra, H.: Western Europe is warming much faster than expected, Clim. Past, 5, 1–12, https://doi.org/10.5194/cp-5-1-2009, 2009. [VERIFY whether this is the intended 2019 citation]
60. World Bank: Global Gas Flaring Reduction Partnership (GGFR), World Bank, Washington, DC, USA, 2023. [REPLACE with the exact dataset/report actually used and provide DOI/URL/access date]
61. World Meteorological Organization: Global Observing System for Climate, World Meteorological Organization, Geneva, Switzerland, 2016. [VERIFY exact report title and edition]
62. Xiang, Y., Zheng, B., Bedra, K. B., Ouyang, Q., Liu, J., and Zheng, J.: Spatial and seasonal differences between near surface air temperature and land surface temperature for Urban Heat Island effect assessment, Urban Clim., 52, 101745, https://doi.org/10.1016/j.uclim.2023.101745, 2023.
63. Xie, S.-P., Deser, C., Vecchi, G. A., Collins, M., Delworth, T. L., Hall, A., Hawkins, E., Johnson, N. C., Cassou, C., Giannini, A., and Watanabe, M.: Towards predictive understanding of regional climate change, Nat. Clim. Change, 5, 921–930, https://doi.org/10.1038/nclimate2689, 2015.
64. Yusuf, N., Okoh, D., Musa, I., Adedoja, S., and Said, R.: A study of the surface air temperature variations in Nigeria, Open Atmos. Sci. J., 11, 54–70, https://doi.org/10.2174/1874282301711010054, 2017.
65. Daniel, O., Yusuf, N., Adedoja, O., Ibrahim, O. A., and Rabiu, B.: Preliminary results of temperature modeling in Nigeria using neural networks, Weather, 70, 336–343, https://doi.org/10.1002/wea.2559, 2015.
66. Okoh, D., Onuorah, L., Rabiu, B., Obafaye, A., Dauda, K., Yusuf, N., and Owolabi, O.: An application of artificial intelligence for investigating the effect of COVID-19 lockdown on three-dimensional temperature variation in equatorial Africa, Geosci. Front., 13, 101318, https://doi.org/10.1016/j.gsf.2021.101318, 2022.
67. Zhou, F., Hagan, D. F. T., Wang, G., Liang, X. S., Li, S., Shao, Y., Yeboah, E., and Wei, X.: Estimating time-dependent structures in a multivariate causality for land–atmosphere interactions, J. Clim., 37, 1853–1876, https://doi.org/10.1175/JCLI-D-23-0207.1, 2024.